Slice imaging: A new approach to ion imaging and velocity mapping

Christoph R. Gebhardt
Institute of Electronic Structure and Lasers, Foundation for Research and Technology–Hellas, P.O. Box 1527, 71110 Heraklion, Greece and Max Planck Institut für Quantenoptik, Garching, Germany

T. Peter Rakitzis
Department of Physics, University of Crete, Heraklion, Greece and Institute of Electronic Structure and Lasers, Foundation for Research and Technology–Hellas, P.O. Box 1527, 71110 Heraklion, Greece

Peter C. Samartzis
Department of Chemistry, University of Crete, Heraklion, Greece and Institute of Electronic Structure and Lasers, Foundation for Research and Technology–Hellas, P.O. Box 1527, 71110 Heraklion, Greece

Vlassis Ladopoulos
Institute of Electronic Structure and Lasers, Foundation for Research and Technology–Hellas, P.O. Box 1527, 71110 Heraklion, Greece

Theofanis N. Kitsopoulos[a)]
Department of Chemistry, University of Crete, Heraklion, Greece and Institute of Electronic Structure and Lasers, Foundation for Research and Technology–Hellas, P.O. Box 1527, 71110 Heraklion, Greece

(Received 7 March 2001; accepted for publication 16 July 2001)

In this article we present a new approach to the already popular methods of ion imaging and velocity mapping. The novelty of this approach is that the speed and angular distributions are measured directly from the images without the need of inverse Abel transformation as in the conventional approaches. This is achieved by using delayed pulsed extraction of the ions following photodissociation and positioning of the nascent products. Delayed pulsed extraction causes a sufficient velocity spread in the ion cloud such that the time width of the ion packet at the detector is on the order of 500 ns. By using a narrow detector time gate ($<$40 ns) we are able to image only the *center slice* of the ion packet. The result is equivalent to that obtained by conventional methods using the inverse Abel transform, however, the artificial noise introduced by this transform is eliminated. The energy resolution of the new approach is at least comparable to that achieved with the velocity mapping technique. © *2001 American Institute of Physics.*
[DOI: 10.1063/1.1403010]

I. INTRODUCTION

In most chemical dynamics experiments the desired quantity to measure is the state-resolved differential cross section $(d\sigma/d\Omega)$.[1] Chandler and Houston introduced ion imaging in 1987,[2] demonstrating for the first time the potential of this method to image scattering processes. A major drawback of the method was its limiting energy resolution (typically 15%–20%) coupled with the ''magical and mysterious'' inverse Abel transformation,[3] which is used to invert the two-dimensional images to give the three-dimensional product speed distribution.[2] Eppink and Parker introduced a remedy to the relatively low resolution in 1997.[4] They used an inhomogeneous extraction field that essentially *focused ion velocities onto the imaging plane*, thus improving the energy resolution by almost an order of magnitude to 2%–5%. However, the necessity for the inverse Abel transform remained.

The use of the Abel transform requires an axis of cylindrical symmetry parallel to the imaging plane. For double resonance experiments, for which photofragment polarization is present, both the photolysis and probe laser polarization directions must be parallel if the inverse Abel transform is to be used. While it is possible to measure the photofragment alignment from Abel-invertible images,[5] it may be more convenient to do so directly from noncylindrical symmetric slice images. Most importantly, certain polarization parameters, most notably the $\mathrm{Im}[\mathbf{a}_1^{(\mathbf{k})}(\parallel,\perp)]$ interference parameter, can *only* be measured from non-Abel-invertible geometries (when the laser polarizations are *not* parallel).

In this article we introduce an alternative method to ion imaging that includes features of velocity mapping and allows the *direct* measurement of $d\sigma/d\Omega$ (without requiring cylindrical symmetry), thereby eliminating the need for inversion techniques such as the Abel transform. In addition, the energy resolution remains comparable to that of velocity mapping. For a test case we study the photodissociation of Cl_2 at 355 nm by probing the ground spin-orbit state of the Cl-atom photofragment.

II. BASIC PRINCIPLES

A. Kinematics of the single uniform acceleration field

This method has been presented in recent reviews,[6,7] however, we would like to go over the kinematics of the

a)Corresponding author; electronic mail: theo@iesl.forth.gr

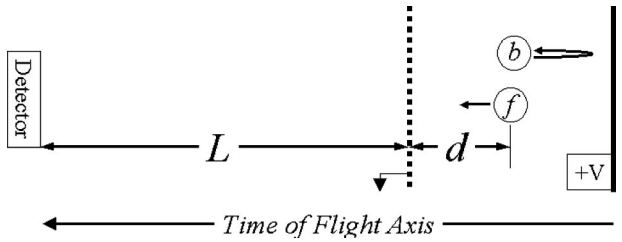

FIG. 1. Typical ion imaging setup, consisting of a homogeneous extraction field $\vec{E}$, a drift region of length L, and a position-sensitive detector (a phosphor screen combined with a CCD camera).

ions, primarily used along the time-of-flight (TOF) axis, since this point is essential in our new approach. In the schematic of a traditional ion imaging setup shown in Fig. 1, ions are created in a homogeneous extraction field E that accelerates them towards the position-sensitive imaging detector. To achieve mass resolution, the extraction field is coupled to a field-free drift region that prolongs the flight time of the ions towards the detector. In addition this drift region allows sufficient time for the ion cloud to expand in diameter thus achieving better speed resolution.

Shown in Fig. 2(a) is a simulation of a photofragment imaging experiment following the photodissociation of a diatomic molecule ($A_2 \rightarrow 2A$). The simulation parameters were chosen to match our experimental conditions: $L=45$ cm, $d=1$ cm, $E=333$ V/cm (acceleration field), $c=1240$ m/s (molecular beam velocity), and $u_0=1668$ m/s (photofragment speed). The spatial extent of the ion cloud at several time

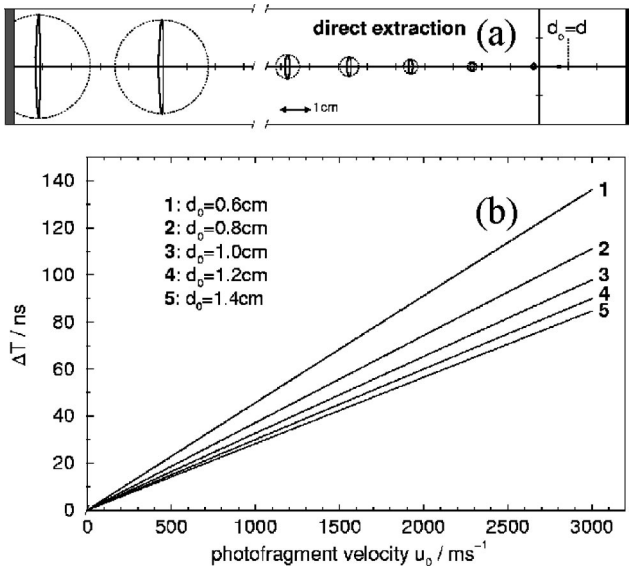

FIG. 2. (a) The upper panel depicts the spatial evolution of the ion cloud on its way to the detector for the case of a dc extraction field. The simulation was performed for ground-state Cl from the photodissociation of Cl_2 at 355 nm ($c=1240$ m/s, $u_0=1700$ m/s, $L=45$ cm, $d_0=d_i=1$ cm, $E=333$ V/cm). The thick line represents the position of the ions at 0, 0.25, 0.50, 1, 1.5, 2.5, 9.75, and 10.75 μs, assuming for simplicity an isotropic photofragment distribution. The dotted circle is included to emphasize the distortion of the ion cloud by the acceleration. (b) The lower panel shows the time width ΔT of the ion cloud at the detector as function of the photofragment velocity. Here, a molecular beam velocity $c=1000$ m/s is assumed. The different curves correspond to different photodissociation and positions d_0 in the extraction region. Similar curves can be obtained by varying the extraction field E, which is equivalent to varying d_0.

intervals is shown. It is immediately obvious that, although the vertical dimension of the ion cloud (Δy) increases considerably during its drift time towards the detector, the horizontal spread (Δx) is nearly invariant. In Fig. 2(b) we plot the temporal spread of the ion packet along the TOF axis as a function of u_0 for the experimental conditions used in the simulation. We observe that ΔT is *extremely* small and varies almost linearly with u_0.

B. Conventional versus pulsed extraction (slice imaging)

As we saw by the discussion in the previous paragraph, when using constant (dc) extraction fields, there is always *crushing* of the ion Newton sphere along the TOF axis. By introducing a time delay τ following the photodissociation and positioning processes, the position of the ions with respect to the extractor grid are

$$d = d_0 - c\tau, \tag{1a}$$

$$d_f = d_0 - (c+u_0)\tau = d - u_0\tau, \tag{1b}$$

$$d_b = d_0 - (c-u_0)\tau = d + u_0\tau, \tag{1c}$$

where d_0 is the initially created position of the ions ($\tau=0$), d_f is the position of the forward-scattered ions, and d_b is the position of the backward-scattered ions after time τ, when the extraction field is switched on. In this case, the temporal spread of the ion cloud along the TOF axis becomes

$$\Delta T = |T_f(d_f, v_f) - T_b(d_b, v_b)|. \tag{2}$$

The influence of the extraction delay τ on the spatial evolution of the ion cloud is presented in the simulation shown in Fig. 3(a). The parameters in this simulation are identical to those used in Fig. 2(a) except that the photodissociation and positioning take place in field-free conditions, i.e., both the repeller and the extractor grid have equal potentials (typically grounded). After a delay of 250 ns the repeller is switched rapidly to 1 kV, so the ions experience an extraction field of 333 V/cm. Following evolution of the width Δx of the ion cloud in Fig. 3(a) we observe the following. During the time delay τ, the ion cloud expands to a specific width ($\sim$0.8 mm), then, following application of the extraction field, Δx decreases, vanishes at the "*geometric* focus" [8] (located a few centimeters behind the extractor grid), and subsequently increases rapidly. This increased spatial width naturally corresponds to some larger spread in the arrival times of the ions. The temporal width ΔT is plotted in Fig. 3(b) as a function of velocity u_0 for various extraction delays. This time delay thus provides a handle for controlling the size of the ion packet along the TOF axis, *while in the meantime ensuring that the perpendicular size of the packet fits on the imaging detector*.

This technique is analogous to *time lag* focusing introduced by Wiley and McLaren in their pioneering paper on TOF mass spectrometry.[8] In their case, however, the time lag was introduced in order to improve the mass resolution and was thus intended to reduce the temporal spread of the ion cloud caused by the *initial* velocity spread. This was

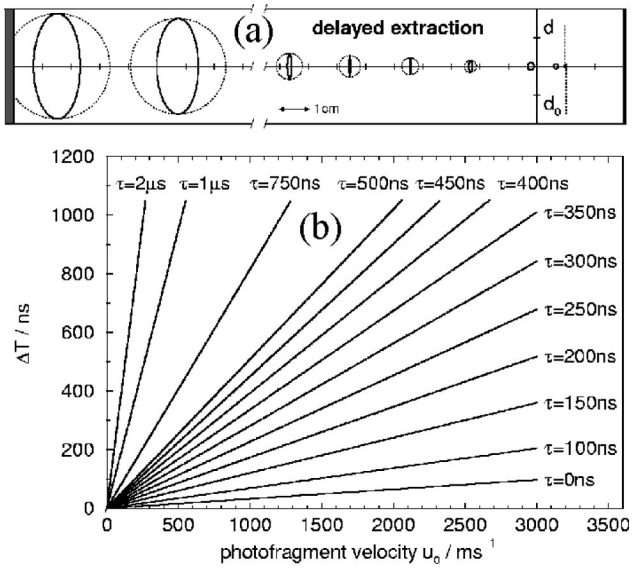

FIG. 3. (a) The upper panel repeats the simulation of Fig. 2(a), however, in this case for delayed extraction of the ion cloud ($\tau = 250$ ns). A space focus appears in the drift region after which the axial width of the ion cloud increases rapidly. (b) The lower panel shows the time width of the ion cloud at the detector as function of the photofragment velocity u_0 ($c = 1000$ m/s). The different curves correspond to different delay times τ. ΔT increases almost linearly over a wide range of photofragment velocities as well as extraction delays. The dependency of ΔT on τ shows a minimum at zero delay times (dc extraction).

achieved by choosing operating conditions such that the spatial focus of the ion cloud occurred at the detector. In our case, it is desirable to operate far from the spatial focus such that the maximal spread in the ion cloud is achieved.

Figure 3(b) shows that a temporal spread on the order of 400 ns can be achieved readily even for extremely low speeds ($u_0 \approx 100$ m/s). Using a moderately fast time gate (<40 ns) on our imaging detector, we are able to image only the *center slice* of the ion cloud which is equivalent to an intensity slice through the three-dimensional photofragment distribution. This image (with in the limit of infinitesimal slicing) is equivalent to the result obtained using the inverse Abel transform in conventional imaging.

III. EXPERIMENT

The apparatus used is described in detail elsewhere.[9] Briefly, a gas sample containing 5% Cl_2 in He is expanded into the source vacuum chamber via a homemade piezoelectrically actuated pulsed-molecular beam operating at 10 Hz. After passing through a skimmer and a collimator, the molecular beam is intersected at right angles by two counterpropagating laser beams. The photolysis laser beam is generated by the third harmonic of a Nd:YAG laser (BMI series 5000). The probe laser beam is generated by a MOPO-SL laser (Spectra Physics 730DT10). The Cl-atom photofragments are ionized using a two-photon resonant transition $4p(^4P_{3/2}) \leftarrow 3p^5(^2P_{3/2})$ 240.53 nm,[10–12] and the ions produced are accelerated towards a homemade ion-imaging detector. Ions of different mass separate according to their time-of-flight during their field-free trajectory en route to the detector. The length of this field-free drift region is ~45 cm.

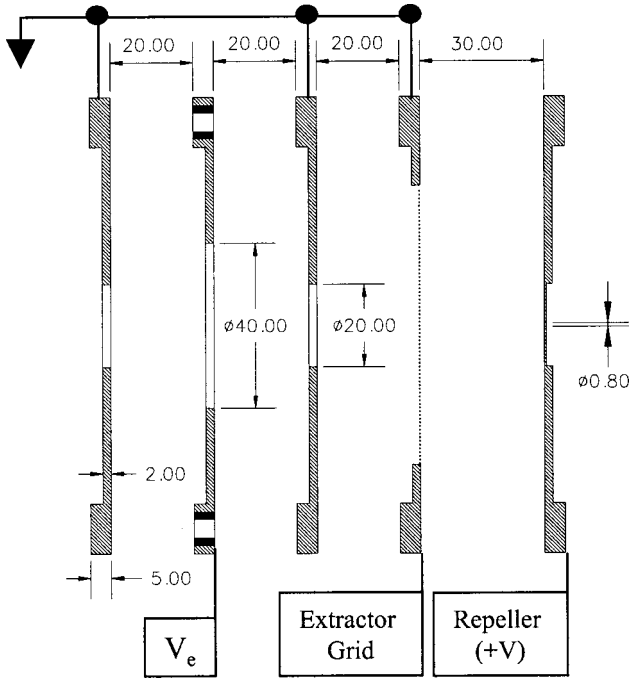

FIG. 4. Scaled schematic of the ion optics (drawing units in mm).

The detector gain is switched on at the proper arrival time for mass selection. Images appearing on the detector anode are recorded using charge coupled device (CCD) camera (Spectra Source).

A schematic of the ion optics used in this experiment is shown in Fig. 4. The optics consist of the repeller electrode that also serves as the molecular beam collimator and the extractor, a grounded flat grid. The quality of the grid is critical since the aberrations introduced by the grid are on the order of the grid hole dimension. For the results presented here the grid used is an electroformed mesh with 333 lines per inch (Buckbey Mears MN-38 BM-0333-01) with a hole size of 58 μm and wire thickness of 12 μm. An Einzel lens assembly is mounted behind the extractor that consists of three slit electrodes. The Einzel lens is used to *velocity map* the photofragments, thus correcting for the finite extent of the interaction volume, and we found that the lens operating voltage is not as critical as in the case of the conventional velocity mapping geometry described in the pioneering paper of Eppink and Parker.[4] We observe that beyond a *minimum* velocity mapping voltage, the lens operates as a geometric focusing lens thus allowing one to zoom in or out of desired parts of the image, without affecting the spatial resolution. For the present geometry we find that for a repeller voltage of 1000 V an Einzel lens voltage of ~150 V is sufficient for velocity mapping to be achieved, and these voltages scale approximately linearly with the repeller voltage.

IV. RESULTS

The photodissociation of Cl_2 at 355 m has been extensively studied. The primary reaction channel is

$$Cl_2 \rightarrow 2Cl(^2P_{3/2}), \tag{3}$$

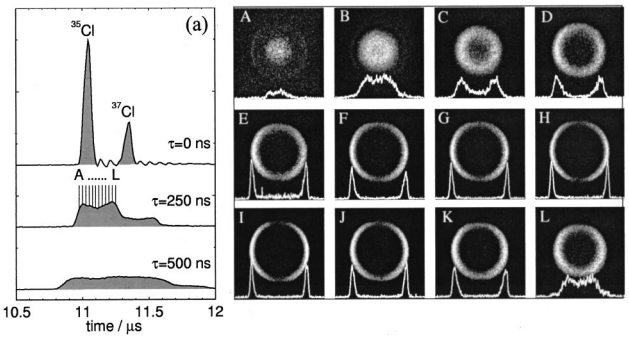

FIG. 5. (a) The left panel depicts time-of-flight mass spectra for chlorine ions for various extraction delays τ. With increasing τ the peaks broaden considerably over time. For a time delay of $\tau=250$ ns the images were taken for individual slices of the ion cloud at the positions indicated by A–L. These images are given in (b) the right panel. Each of them was normalized to increase the contrast for easier visualization. The relative signal intensities are contained in the overlaid curves, which represent horizontal cuts through the center of the image (summed over five adjacent rows).

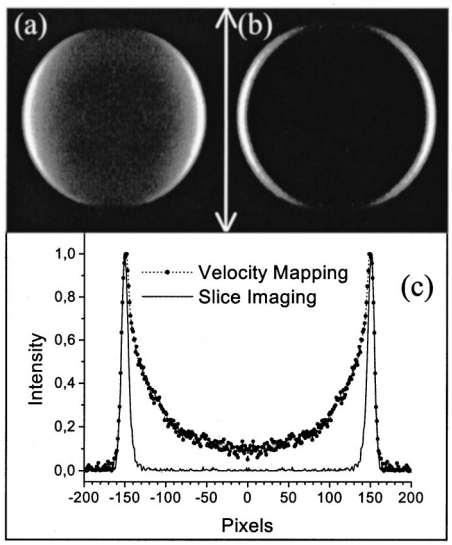

FIG. 6. Comparison between conventional ion imaging and slice imaging. (a) Reproduction of a typical ^{35}Cl photofragment image (see Ref. 14) obtained under velocity mapping conditions. (b) Image obtained using the slice imaging technique. It corresponds to image H in Fig. 5(b). The arrow indicates the polarization axis of the photodissociation and ionization lasers. (c) The lower panel compares intensity profiles for cuts along the equator of the two images above.

with a branching ratio of greater that 99%.[13,14] The transition is a perpendicular one as the molecule is excited from a $X(0_u^+,\Omega=0)$ ground state to the $C(1_u,\Omega=1)$ state. This means that the transition dipole for this excitation lies perpendicular to the molecular bond axis so that a molecule will have the maximum absorption probability when it lies perpendicular to the laser polarization (electric field direction).[15]

A. Slice imaging

The characteristics of slice imaging are summarized in Fig. 5. The region of interest of the mass time-of-flight spectrum is shown in Fig. 5(a). For $\tau=0$ the mass spectrum consists of two narrow peaks which correspond to ^{35}Cl and ^{37}Cl. As predicted by the simulation in Fig. 3(a), increasing the time delay to 250 ns causes the two peaks to become broader and to start to be partially resolved. A further increase in the time delay yields a broad unresolved mass peak. Hence, although increasing the time delay would allow more simple *slicing*, when multiple isotopes of the species being probed are present, the upper limit in the time delay is set by the amount of overlapping between the isotope peaks. We wish to point out here that, even in the absence of any isotopes, if the delay times become too large, then the dimensions of the ion cloud become comparable to the ion optic dimensions. When this happens, distortions due to edge effects become apparent.

A series of images are presented in Fig. 5 that were acquired at 25 ns time intervals, indicated by the comb structure in Fig. 5(a), thus slicing through the ^{35}Cl ion cloud for $\tau=250$ ns. The polarization of the photolysis laser for all the images presented in this article is linear and vertical with respect to the figure frame. Image A is the fastest part of the ion cloud and corresponds to fragments that are initially backscattered. The appearance of a bright center core is what one expects for a sphere with an anisotropy parameter of $\beta=-1$,[14,15] i.e., maximum intensity along the equator. The faint signal at larger radii is some leakage of the entire Cl ion cloud because the 1100 dc voltage on the microchannel plate (MCP) stack is sufficient to detect some ions. While slicing at longer arrival times, the radius of the image increases and becomes brighter on the edge and hollow in the center. *The image radius becomes maximum for image H and this image corresponds to the center slice*. The reverse trend follows as we continue to probe at even longer arrival times, and eventually we start *slicing* mass ^{37}Cl. Thus we conclude that a time delay of $\tau=250$ ns is sufficient for slice imaging the ^{35}Cl photofragments.

B. Conventional velocity mapping versus slice imaging

Figure 6(a) shows an image of a typical ^{35}Cl photofragment obtained using conventional velocity mapping, and this image appears to be consistent with the predictions above ($\beta=-1$) and a detailed analysis of it is presented elsewhere.[14] After appropriate image processing the speed and angular distributions were determined and they are presented in Figs. 7 and 8.[6,16] Figure 6(b) is the center slice image, H [Fig. 5(b)].

The intensity cuts along the equator of the two images are presented in Fig. 6(c). For conventional velocity mapping the profile is characteristic of a $\beta=-1$,[15] and one major advantage of slice imaging becomes immediately apparent. The long tail inherent in the projection of the entire photofragment Newton sphere was eliminated when performing slice imaging. The sharpness of the outer edges is identical thus indicating that the grid used in the extractor is of sufficient quality that it does not degrade the resolution of the image obtained, at least in comparison to conventional velocity mapping. In considering a situation in which multiple channels are involved, a very weak interior peak can be hidden under the tail of the outer peak and will thus be missed when performing the inverse Abel transform. In the case of slice imaging, however, such a situation is circumvented.

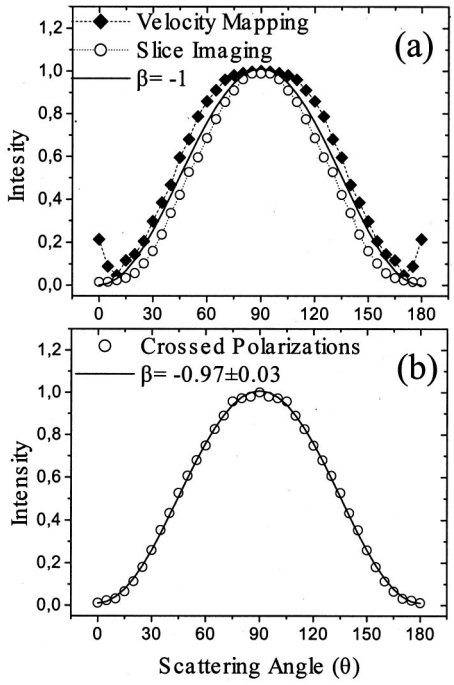

FIG. 7. (a) Angular distributions obtained with conventional and with slice imaging when the polarizations of the photolysis and probe lasers are parallel. Also shown is a fit to both data for $\beta=-1$. (b) Angular distributions obtained with slice imaging when the polarizations of the photolysis and probe lasers are crossed.

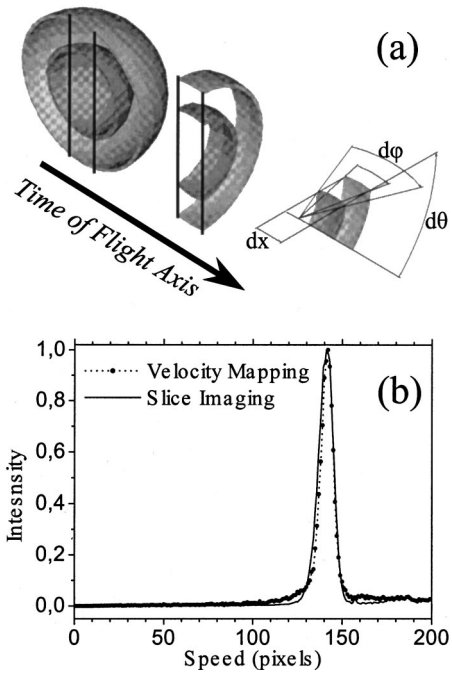

FIG. 8. (a) Schematic of the slice imaging method. The center part of two Newton spheres is cut out by means of a gated detector. The images obtained in this way are a projection of a very finite strip of the Newton sphere. (b) The lower panel compares the speed distributions obtained with velocity mapping and with slice imaging. The curves correspond to the images in Fig. 6.

Recently, a further improvement in velocity mapping involved the use of an ion event counting acquisition method,[17,18] whereby during the acquisition one determines the *centroid* of each ion event (blob/spot), sets the intensity of the *centroid pixel* to 1 and all the other pixels to 0. Although this is an excellent way to correct detector inhomogeneities, it takes a very long time to acquire enough *centroid statistics* to fill the entire image and thus enable one to perform the inverse Abel transform. The usual practice is to *blur* the pixilated image with some Gaussian function (typically 3×3 pixels) and subsequently perform the inverse Abel transform. This procedure however can be dangerous because the inverse Abel transform requires that *the entire phase space of the photofragment Newton sphere be sampled, and this is NOT the same as smoothing sharp features using a Gaussian function*. If however one were to apply the event counting procedure to slice imaging since the inverse Abel transformation will not be applied, no smoothing of the data that artificially degrades the resolution would be needed.

C. Extracting angular distributions from slice images

The angular distribution $I(\theta)$ for *each speed* appearing in a slice image is obtained by integrating the image in the same manner as that in the case of the inverse Abel transformed image.[16] That is,

$$I(\theta)=\frac{N(\theta)}{\Delta\theta}, \tag{4}$$

where $N(\theta)$ is the total pixel intensity in a radial sector centered at the center of mass of the image, with an angle $\Delta\theta$.

Three distinct advantages of the slice imaging technique include the following.

(1) The noise introduced by the inverse Abel transform, particularly that along the symmetry axis, is eliminated. This feature is demonstrated in Fig. 7(a) where the angular distribution obtained using the inverse Abel transform shows artificial noise near the symmetry axis, while this noise is *absent* in the angular distribution determined from slice imaging.

(2) Abel-invertible geometries are no longer a prerequisite. This is a tremendous asset when photofragment alignment and orientation are present. For the case in hand, it has been shown that the Cl photofragments are aligned.[19–21] This would lead to deviation from the limiting β value of -1 when the photolysis and probe polarizations are parallel, as is evident in both angular distributions in Fig. 7(a). However, if one rotates the probe polarization 90° with respect to the imaging plane (such that the angle between the probe polarization and all the photofragment velocities detected in the slice image is approximately 90°), then for this system, the true β value is measured. This is confirmed in Fig. 7(b) where the fit to the data yields $\beta=-0.97\pm0.03$.

(3) It is no longer necessary to have all velocities of the photofragmentation process on the *same image* since the inverse Abel transform is no longer needed. Hence one can *expand* the image on the detector as much as desired (thereby losing the fast components) without any loss of information for the slow components. In addition, the use of a homogeneous electric field makes it possible to

operate even at very low repeller voltages (<100 V), which is not possible with conventional velocity mapping because of lens aberrations.

D. Extracting speed distributions from slice images

Unlike the inverse Abel transform which yields an image that represents the intensity slice along a plane containing the symmetry axis, slice images are actually a projection of a very finite stripe of the Newton sphere. In order to obtain the speed distribution with the usual $\rho \sin\theta$ weighting of each pixel,[16] we must first divide out by the *azimuthal contribution to the solid angle subtended at each radius*. Shown in Fig. 8(a) is the slicing of two concentric Newton spheres. Assuming that the lab velocity for the near perpendicular direction of each concentric ion cloud is about the same, then the *spatial extent* (dx) of the slice for each Newton sphere along the TOF axis will be approximately a constant for all radii. If the photolysis laser polarization is parallel to the *column direction* of the data image, then for *a row of data*, the *slice* intensity $I_R(\theta)$ can be related to corresponding intensity obtained from the conventional inverse Abel transform $I_R^A(\rho)$ as follows:

$$I_R(\rho) \approx I_R^A(\rho)dx \Rightarrow I_R^A(\rho) \propto I_R(\rho). \tag{5}$$

Hence we observe that the procedure for obtaining the speed distribution for slice images is identical to the procedure used for conventional ion imaging and or velocity mapping, i.e., we weigh each pixel by $\rho \sin\theta$.

The speed distributions for the Cl atoms determined using velocity mapping and slice imaging are presented in Fig. 8(b). The widths of the two distributions are comparable. However, as we explained earlier, we believe that the *effective* resolution of slice imaging is in principle better than that of conventional imaging since the tail in the intensity profile of the image projection is not present in the slice image. One can of course perform peak shaping to the intensity profile of the slice image to enhance the resolution even more, but the beauty of this new method lies in its direct determination of both the speed and angular distribution without any mathematical transformation.

ACKNOWLEDGMENTS

The authors thank Giorgos Gousis for outstanding technical support in building the high voltage pulsers. This work was conducted at the Ultraviolet Laser Facility operating at FORTH-IESL (Improving Human Potential-Transnational Access to Major Research Infrastructures, HPRI-CT-1999-00074) and was supported by TMR Network IMAGINE ERB 4061 PL 97-0264.

[1] R. D. Levine and R. B. Bernstein, *Molecular Reaction Dynamics and Chemical Reactivity* (Oxford University Press, Oxford, 1987).
[2] D. W. Chandler and P. L. Houston, J. Chem. Phys. **87**, 1445 (1987).
[3] R. N. Bracewell, *The Fourier Transform and Its Applications* (McGraw–Hill, New York, 1986).
[4] A. T. J. B. Eppink and D. H. Parker, Rev. Sci. Instrum. **68**, 3477 (1997).
[5] T. P. Rakitzis, P. C. Samartzis, and T. N. Kitsopoulos Phys. Rev. Lett. (submitted).
[6] A. J. R. Heck and D. W. Chandler, Annu. Rev. Phys. Chem. **46**, 335 (1995).
[7] A. G. Suits and R. E. Continetti, *Imaging in Chemical Dynamics* Symposium Series No. 770 (American Chemical Society, Washington, DC, 2001).
[8] W. C. Wiley and I. H. McLaren, Rev. Sci. Instrum. **26**, 1150 (1955).
[9] P. C. Samartzis, I. Sakellariou, T. Gougousi, and T. N. Kitsopoulos, J. Chem. Phys. **107**, 43 (1997).
[10] S. Arepalli, N. Presser, D. Robie, and R. J. Gordon, Chem. Phys. Lett. **118**, 88 (1985).
[11] C. E. Moore, *Atomic Energy Levels as Derived from the Analyses of Optical Spectra* (Washington, DC, U.S. Dept. of Commerce, 1949).
[12] W. R. Simpson, T. P. Rakitzis, S. A. Kandel, J. Orr-Ewing, and R. N. Zare, J. Chem. Phys. **103**, 7313 (1995).
[13] Y. Matsumi, K. Tonokura, and M. Kawasaki, J. Chem. Phys. **97**, 1065 (1992).
[14] P. C. Samartzis, B. L. G. Bakker, T. P. Rakitzis, D. H. Parker, and T. N. Kitsopoulos, J. Chem. Phys. **110**, 5201 (1999).
[15] R. N. Zare, Mol. Photochem. **4**, 1 (1972).
[16] D. W. Chandler, T. N. Kitsopoulos, M. A. Buntine, D. P. Baldwin, R. I. McKay, A. J. R. Heck, and R. N. Zare, in *Gas-Phase Chemical Reaction Systems: Experiments and Models 100 Years After Max Bodenstein*, edited by J. Wolfrum, H.-R. Volpp, R. Rannacher, and J. Warnatz, Springer Series in Chem. Phys. (Springer, Berlin, 1996).
[17] L. J. Rogers, M. N. R. Ashfold, Y. Matsumi, M. Kawasaki, and B. J. Whitaker, Chem. Phys. Lett. **258**, 159 (1996).
[18] B. Y. Chang, R. C. Hoetzlein, J. A. Mueller, J. D. Geiser, and P. L. Houston, Rev. Sci. Instrum. **69**, 1665 (1998).
[19] Y. Wang, H. P. Loock, J. Cao, and C. X. W. Qian, J. Chem. Phys. **102**, 808 (1995).
[20] A. S. Bracker, E. R. Wouters, A. G. Suits, Y. T. Lee, and O. S. Vasyutinskii, Phys. Rev. Lett. **80**, 1626 (1998).
[21] T. P. Rakitzis, S. A. Kandel, A. J. Alexander, Z. H. Kim, and R. N. Zare, J. Chem. Phys. **110**, 3151 (1999).